

AN ENERGY METHOD FOR PREDICTING AND SUPPRESSING THE INSTABILITY OF A THREE-DIMENSIONAL THERMOACOUSTIC COUPLING SYSTEM WITH A MICRO-PERFORATED PLATE

XUE XING, BINGJIE MA

*Shanghai Marine Diesel Engine Research Institute, Shanghai, China, and
National Engineering Research Center of Special Equipment and Power System for Ship and Marine Engineering,
Shanghai, China
corresponding author Xue Xing, e-mail: xingxue@hrbeu.edu.cn*

JINGTAO DU, YANG LIU, ZHIGANG LIU

College of Power and Energy Engineering, Harbin Engineering University, Harbin, China

XIAO HAN

Shanghai Marine Diesel Engine Research Institute, Shanghai, China

The Micro-Perforated Plate (MPP) is widely used in the noise control field with advantages of high temperature resistance and being suitable for high-speed flow fields. In this paper, an analytical model of the three-dimensional thermoacoustic coupling system suppressed by the MPP is established through the energy principle and Rayleigh-Ritz method. A modified Fourier series will be applied to characterize the sound pressure distribution function to meet arbitrary impedance boundary conditions. Based on the sound intensity and divergence, the energy transmission path and distribution law of energy sources and traps are analyzed. The suppression mechanism of a MPP on the thermoacoustic instability is revealed.

Keywords: thermoacoustic coupling system, micro-perforated plate, modified Fourier series

1. Introduction

The thermoacoustic coupling oscillation occurring in combustion systems of gas turbines seriously affects quietness and operation reliability of the equipment (Dowling and Mahmoudi, 2015; Seo, 2003; Lefebvre and Ballal, 2010). The Micro-Perforated Plate (MPP) has the advantage of not being limited by high temperature, high speed and other harsh environments (Zhang, 2020; Schönfeld and Poinot, 1999; Armitage *et al.*, 2004; Schuller *et al.*, 2003). Therefore, the MPP has attracted attention in the thermoacoustic oscillation control field. However, the effective handling of thermoacoustic coupling system with MPPs in terms of modelling, optimization and mechanism exploration is technically challenging.

At present, scholars have carried out a series of studies on suppression of thermoacoustic coupling oscillation by MPPs. Eldredge and Dowling *et al.* (2003) proposed that the perforated structure on the combustion chamber wall can be simplified as a perforated plate model. Ma (1975) pointed out that the MPP sound absorption structure is a resonant sound absorber which is characterized by a wide frequency band, simple structure and can be used in special environments. Sun (2010) used CFD to simulate the thermoacoustic system and discussed the influence of structural parameters such as perforation rate on the thermoacoustic oscillation characteristics. Chu and Xu (2016) carried out numerical simulation analysis using CAA,

the three-dimensional (3D) acoustic equation was solved to predict the modal information of the thermoacoustic system, and then the inhibition effect of the MPP on unstable modes was simulated. The above investigation proves that, most of the research on suppression of thermoacoustic oscillation by MPPs is still limited to experimental methods and numerical simulation methods. In the experiment, the thermoacoustic coupling oscillation phenomenon is suppressed through empirical debugging. In the numerical simulation, the appropriate MPP parameters and installation positions are determined through a large number of parameter analysis, and there is a lack of understanding of the control mechanism of thermoacoustic coupling oscillation.

Motivated by this, this paper proposes a semi-analytical technique based on the energy principle and Rayleigh Ritz method to reveal the characteristic of thermoacoustic coupling phenomenon and realize effective suppression of thermoacoustic oscillation. The 3D thermoacoustic coupling system is established, taking into account arbitrary impedance boundary conditions and the MPP. The system structure can be decomposed by a substructure method. To ensure smoothness of the field function, a modified Fourier series enriched with auxiliary polynomial terms is constructed for decomposition of the sound pressure. Numerical analyses are performed with a particular focus on the sound field energy transmission path and the control strategy of the MPP on the thermoacoustic coupling instability.

2. Theoretical model

A 3D thermoacoustic coupling system with arbitrary impedance boundary conditions, variable cross-section and MPP is shown in Fig. 1a. According to characteristics of the complex cavity structure, it can be divided into acoustic cavity substructures TAC_1 and TAC_2 , which are connected by auxiliary air plates TAA at the interface, as shown in Fig. 1b. The heat source is located in TAC_2 , and the MPP can be located at an arbitrary position on the wall. Assuming that the MPP at $y = 0$, the starting coordinate of MPP is expressed as $(x_m, 0, z_m)$.

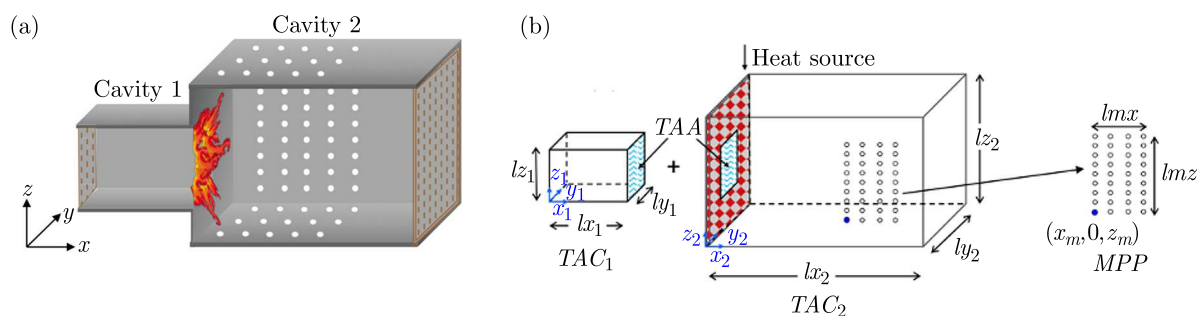


Fig. 1. The 3D thermoacoustic coupling system with the MPP

2.1. Sound pressure distribution function of the acoustic cavity substructure and the displacement function of an auxiliary air plate at the interface

The 3D modified Fourier series expression (Du *et al.*, 2011) is used to describe the sound pressure distribution, expressed as p_{c1} and p_{c2} , respectively

$$\begin{aligned}
 p_{c_i}(x, y, z) = & \sum_{m_x^{c_i}=0}^{\infty} \sum_{m_y^{c_i}=0}^{\infty} \sum_{m_z^{c_i}=0}^{\infty} A_{m_x^{c_i} m_y^{c_i} m_z^{c_i}} \cos \lambda_{m_x^{c_i}} x \cos \lambda_{m_y^{c_i}} y \cos \lambda_{m_z^{c_i}} z \\
 & + \sum_{m_y^{c_i}=0}^{\infty} \sum_{m_z^{c_i}=0}^{\infty} \left[\underbrace{B_{m_y^{c_i} m_z^{c_i}} \xi_{1c_i}(x)}_{x_i=0} + \underbrace{C_{m_y^{c_i} m_z^{c_i}} \xi_{2c_i}(x)}_{x_i=l_{x_i}} \right] \cos \lambda_{m_y^{c_i}} y \cos \lambda_{m_z^{c_i}} z \\
 & + \sum_{m_x^{c_i}=0}^{\infty} \sum_{m_z^{c_i}=0}^{\infty} \left[\underbrace{D_{m_x^{c_i} m_z^{c_i}} \xi_{1c_i}(y)}_{y_i=0} + \underbrace{E_{m_x^{c_i} m_z^{c_i}} \xi_{2c_i}(y)}_{y_i=l_{y_i}} \right] \cos \lambda_{m_x^{c_i}} x \cos \lambda_{m_z^{c_i}} z \\
 & + \sum_{m_x^{c_i}=0}^{\infty} \sum_{m_y^{c_i}=0}^{\infty} \left[\underbrace{F_{m_x^{c_i} m_y^{c_i}} \xi_{1c_i}(z)}_{z_i=0} + \underbrace{G_{m_x^{c_i} m_y^{c_i}} \xi_{2c_i}(z)}_{z_i=l_{z_i}} \right] \cos \lambda_{m_x^{c_i}} x \cos \lambda_{m_y^{c_i}} y
 \end{aligned} \tag{2.1}$$

where $i = 1, 2$, $\lambda_{m_x^{c_i}} = m_x^{c_i} \pi / (l_{x_i})$, $\lambda_{m_y^{c_i}} = m_y^{c_i} \pi / (l_{y_i})$, $\lambda_{m_z^{c_i}} = m_z^{c_i} \pi / (l_{z_i})$. The specific expression of the boundary complementary function shown as the x -axis is

$$\xi_{1c_i}(x) = x \left(\frac{x}{l_{x_i}} - 1 \right)^2 \quad \xi_{2c_i}(x) = \frac{x^2}{l_{x_i}} \left(\frac{x}{l_{x_i}} - 1 \right) \tag{2.2}$$

In the analysis, the TAA can be regarded as a 2D elastic thin plate structure, and the sound field transfer between the adjacent acoustic cavity substructures is transformed into bending vibration. The bending vibration displacement of TAA is expressed by 2D Fourier series, i.e.

$$w_a(y, z) = \sum_{m_y^a=0}^{\infty} \sum_{m_z^a=0}^{\infty} w_{m_y^a m_z^a} \cos \lambda_{m_y^a} y \cos \lambda_{m_z^a} z \tag{2.3}$$

where $\lambda_{m_y^a} = m_y^a \pi / (l_{y_1})$, $\lambda_{m_z^a} = m_z^a \pi / (l_{z_1})$.

2.2. Lagrange function of the acoustic cavity substructure and the auxiliary air plate at the interface

After obtaining the sound pressure distribution of TAC and the displacement function of TAA, it is necessary to further obtain all the unknown Fourier coefficients. The characteristic equation of the thermoacoustic coupling system with the MPP will be constructed using the energy principle and Rayleigh-Ritz method. Writing Lagrangian for TAC and TAA

$$\begin{aligned}
 L_{c_1} &= V_{c_1} - T_{c_1} - W_{end1} - W_{a\&c_1} - W_S \\
 L_{c_2} &= V_{c_2} - T_{c_2} - W_{end2} - W_{MPP} - W_{a\&c_2} - W_{heat} \\
 L_a &= V_a - T_a + W_{c_1\&a} + W_{c_2\&a}
 \end{aligned} \tag{2.4}$$

where V_c, T_c are the potential energy and kinetic energy of TAC, W_{end1} and W_{end2} are the work done by the impedance end of TAC, W_{heat} is the work done by the heat source, $W_{a\&c}$ is the work done by bending vibration of TAA to TAC.

The potential energy and kinetic energy of TAC₁ and TAC₂ are

$$\begin{aligned}
 V_i &= \frac{1}{2\rho_i c_i^2} \int_{V_i} p_i^2(x, y, z) dV_i = \frac{1}{2\rho_i c_i^2} \int_0^{l_{z_i}} \int_0^{l_{y_i}} \int_0^{l_{x_i}} p_i^2(x, y, z) dx dy dz \quad i = 1, 2 \\
 T_i &= \frac{1}{2\rho_i \omega^2} \int_{V_i} (\text{grad } p)^2 dV_i = \frac{1}{2\rho_i \omega^2} \int_0^{l_{z_i}} \int_0^{l_{y_i}} \int_0^{l_{x_i}} \left[\left(\frac{\partial p_i}{\partial x} \right)^2 + \left(\frac{\partial p_i}{\partial y} \right)^2 + \left(\frac{\partial p_i}{\partial z} \right)^2 \right] dx dy dz
 \end{aligned} \tag{2.5}$$

The works done by the auxiliary air plate to the acoustic cavity substructure are

$$\begin{aligned}
 W_{a\&c_1} &= \int_{S_a} p_1(x, y, z) \Big|_{x=l_{x_1}} w_a dS_a = \int_0^{l_{z_1}} \int_0^{l_{y_1}} p_1(x, y, z) \Big|_{x=l_{x_1}} w_a dy dz \\
 W_{a\&c_2} &= \int_{S_a} p_2(x, y, z) \Big|_{x=0} w_a dS_a = \int_{\frac{l_{z_2}}{2} - \frac{l_{z_1}}{2}}^{\frac{l_{z_2}}{2} + \frac{l_{z_1}}{2}} \int_{\frac{l_{y_2}}{2} - \frac{l_{y_1}}{2}}^{\frac{l_{y_2}}{2} + \frac{l_{y_1}}{2}} p_2(x, y, z) \Big|_{x=0} w_a dy dz
 \end{aligned} \tag{2.6}$$

The work done by the inlet impedance of the acoustic cavity substructure TAC₁

$$W_{end1} = -\frac{1}{2} \int_{S_0} \frac{p_1(x, y, z)^2}{j\omega Z_0} \Big|_{x=0} dS_0 = -\frac{1}{2} \int_0^{l_{z_1}} \int_0^{l_{y_1}} \frac{p_1(x, y, z)^2}{j\omega Z_0} \Big|_{x=0} dy dz \tag{2.7}$$

The work done by the outlet impedance of the acoustic cavity substructure TAC₂

$$W_{end2} = -\frac{1}{2} \int_{S_L} \frac{p_2(x, y, z)^2}{j\omega Z_L} \Big|_{x=l_{x_2}} dS_L = -\frac{1}{2} \int_0^{l_{z_2}} \int_0^{l_{y_2}} \frac{p_2(x, y, z)^2}{j\omega Z_L} \Big|_{x=l_{x_2}} dy dz \tag{2.8}$$

The equivalent impedance of MPP can be expressed as

$$Z_{MPP} = \frac{32\mu t_h}{\delta_h \rho c d_h^2} \left[\left(1 + \frac{K^2}{32}\right)^{\frac{1}{2}} + \frac{\sqrt{2}}{32} K \frac{d_h}{t_h} \right] + j \frac{\omega t_h}{\delta_h c} \left[1 + \left(9 + \frac{K^2}{32}\right)^{-\frac{1}{2}} + 0.85 \frac{d_h}{t_h} \right] \tag{2.9}$$

where μ is the aerodynamic viscosity, δ_h is the perforation rate, d_h is the hole diameter, and t_h is the plate thickness.

The acoustic effect of the MPP is characterized by distribution impedance, and the energy dissipation in the sound field can be expressed as

$$W_{MPP} = -\frac{1}{2} \int_{S_{MPP}} \frac{p_2(x, y, z)^2}{j\omega Z_{MPP}} dS_{MPP} \tag{2.10}$$

The work done by the heat source can be obtained

$$W_{heat} = \frac{1}{2} \frac{\gamma - 1}{\rho_2 c_2^2} \int_0^{l_{z_2}} \int_0^{l_{y_2}} \frac{p_2(x_q) q}{j\omega} dy dz \quad q(x, t) = \frac{Q(t)}{S} \delta(x - x_q) \tag{2.11}$$

in which γ is the ratio of specific heats, and q represents the heat release rate per unit area, Q is the heat release rate, x_q is the heating position.

The potential and kinetic energy of the auxiliary air plate at the interface are respectively

$$\begin{aligned}
 V_a &= \frac{D}{2} \int_0^{l_{z_1}} \int_0^{l_{y_1}} \left[\left(\frac{\partial^2 w_a}{\partial y^2}\right)^2 + \left(\frac{\partial^2 w_a}{\partial z^2}\right)^2 + 2\mu \frac{\partial^2 w_a}{\partial y^2} \frac{\partial^2 w_a}{\partial z^2} + 2(1 - \mu) \left(\frac{\partial^2 w_a}{\partial y \partial z}\right)^2 \right] dy dz \\
 T_a &= \frac{1}{2} \omega^2 \rho_a \delta_a \int_0^{l_{z_1}} \int_0^{l_{y_1}} w_a^2 dy dz
 \end{aligned} \tag{2.12}$$

where D , μ , ρ_a , δ_a are the bending stiffness, Poisson's ratio, mass density and thickness of the air plate. The temperature of air plate is consistent with the temperature of the acoustic cavity, the particle velocity is determined by the current position, and can be obtained according to the Euler equation of motion.

2.3. Characteristic equation of the thermoacoustic coupling system

In numerical calculation, the Fourier series of the acoustic cavity substructure is truncated at $m_x = M_x$, $m_y = M_y$, $m_z = M_z$, and the Fourier series of the auxiliary air plate is truncated at $m_a = M_a$. Applying the Lagrange equation and Rayleigh-Ritz method with respect to all the unknown coefficients yields the following condensed matrix form

$$\begin{aligned} & (\mathbf{K}_{c1} - \omega \mathbf{Z}_{c1} - \omega^2 \mathbf{M}_{c1}) \mathbf{P}_{c1} + \omega^2 \mathbf{C}_{a\&c1} \mathbf{W}_a = \mathbf{Q}_s \\ & \left(\mathbf{K}_{c2} - \frac{1}{2} \frac{b(\gamma - 1)}{\rho^2 c^2 S (1 + j\omega t)} \mathbf{R} - \omega \mathbf{Z}_{MPP} - \omega \mathbf{Z}_{c2} - \omega^2 \mathbf{M}_{c2} \right) \mathbf{P}_{c2} + \omega^2 \mathbf{C}_{a\&c2} \mathbf{W}_a = \mathbf{0} \\ & (\mathbf{K}_a - \omega^2 \mathbf{M}_a) \mathbf{W}_a + \mathbf{C}_{c1\&a} \mathbf{P}_{c1} + \mathbf{C}_{c2\&a} \mathbf{P}_{c2} = \mathbf{0} \end{aligned} \quad (2.13)$$

where \mathbf{K}_{c1} , \mathbf{K}_{c2} , \mathbf{K}_a are the stiffness matrices of the substructures, \mathbf{M}_{c1} , \mathbf{M}_{c2} , \mathbf{M}_a are the mass matrices of substructures, $\mathbf{C}_{a\&c}$ and $\mathbf{C}_{c\&a}$ are the auxiliary matrices of the interaction between TAC and TAA, \mathbf{Z}_{c1} , \mathbf{Z}_{c2} are the boundary impedance work matrices, \mathbf{Z}_{MPP} is the MPP work matrix, \mathbf{R} is the heat source work matrix, \mathbf{P}_c and \mathbf{W}_a are unknown Fourier coefficient vectors.

Considering that the auxiliary air plate at the interface is a virtual structure, the thickness of the air plate in the numerical calculation is a small value ($\delta_a = 10^{-6}$ m), and bending stiffness $D = 0$. Therefore, the potential energy of the air plate is $V_a = 0$, and Eq. (2.13)₃ can be simplified to

$$-\omega^2 \mathbf{M}_a \mathbf{W}_a + \mathbf{C}_{c1\&a} \mathbf{P}_{c1} + \mathbf{C}_{c2\&a} \mathbf{P}_{c2} = \mathbf{0} \quad (2.14)$$

Dynamic equations (2.13) and (2.14) are simultaneously established, and the matrix characteristic equation for the thermoacoustic coupling system can be obtained

$$(\mathbf{K} - \omega \mathbf{Z} - \omega^2 \mathbf{M} - \omega^2 \mathbf{X}) \mathbf{P} = \mathbf{Q} \quad (2.15)$$

The coupling characteristics can be obtained by solving the system matrix eigenequation. The most important is that ω is a complex number, whose real part, denoted by $\text{Re}(\omega)$, represents the oscillation frequency, and the minus of the imaginary part of ω , $-\text{Im}(\omega)$ is the growth rate of the oscillation amplitude. The growth rate greater than zero means the unstable mode, less than zero is the stable mode.

3. Numerical simulation and analysis

3.1. Model validation

When the heat source is not considered, the thermoacoustic coupling system degenerates into a pure acoustic system, and the matrix characteristic equation (2.15) of TAC₂ degenerates to

$$(\mathbf{K}_{c2} - \omega \mathbf{Z}_{MPP} - \omega \mathbf{Z}_{c2} - \omega^2 \mathbf{M}_{c2}) \mathbf{P}_{c1} + \omega^2 \mathbf{C}_{a\&c2} \mathbf{W}_a = \mathbf{0} \quad (3.1)$$

Dynamic equations (2.13)₁, (2.14) and (3.1) are simultaneously established, and the matrix characteristic equation for the pure acoustic system can be obtained.

The geometric parameters of TAC are $l_{x1} = 0.3$ m, $l_{y1} = 0.5$ m, $l_{z1} = 0.5$ m, $l_{x2} = 0.7$ m, $l_{y2} = 1$ m, $l_{z2} = 1$ m. The right end of TAC₂ is the pressure release boundary. Three MPPs are selected, $l_{my} = 0.1$ m, 0.3 m and 0.5 m, respectively, and $l_{mz} = l_{z2}$. MPP is on $y = 0$, and the starting coordinates are $(0.9$ m, $0, 0)$, $(0.7$ m, $0, 0)$ and $(0.5$ m, $0, 0)$ in turn. The MPP structure parameters are shown in Table 1. COMSOL Multiphysics software has been used for comparative verification of thermoacoustic coupling systems. Firstly, a variable cross-section three-

-dimensional thermoacoustic coupling system is established, and pressure acoustics and frequency domain modules are used to calculate the thermoacoustic coupling characteristics, including the variable cross-section acoustic cavity, heat source domain, wall distributed impedance, and inlet and outlet boundary impedance. The heat source is introduced in the form of local integration, and the coupled iterative calculation between the heat source and the acoustic system is formed by using local ordinary differential and differential algebra equations. The finite element mesh division of its structure, includes 33379 tetrahedral elements, 8232 triangular elements, and 480 edge elements. The average element mass is 0.584, and the mesh volume is 0.85 m³. The grid at the heat source region is dense, with 9318 tetrahedrons, an average element mass of 0.4047, and a grid volume of 0.01 m³. The current modal frequencies of the 3D acoustic cavity with MPPs are shown in Table 2. Figure 2 shows a comparison of modal shapes between the results from the current method and FEM.

Table 1. MPP structure parameters

MPP parameters	Value	Unit
Perforation rate	1.2	%
Orifice diameter	0.001	m
Panel thickness	0.003	m
Aerodynamic viscosity	1.789E-5	Pa·s

Table 2. Comparison of modal frequencies of the acoustic system with different MPPs [Hz]

Order	$l_{my} = 0.1$ m		$l_{my} = 0.3$ m		$l_{my} = 0.5$ m	
	Current	FEM	Current	FEM	Current	FEM
1	181.66	182.19	183.70	183.91	187.58	187.29
2	181.96	182.49	187.53	186.74	192.03	191.74
3	202.94	202.48	223.47	222.68	249.22	248.93
4	254.01	253.54	268.04	268.25	284.18	283.89
5	278.23	278.76	278.37	277.58	293.95	293.66
6	307.02	307.55	309.39	309.60	308.88	309.59

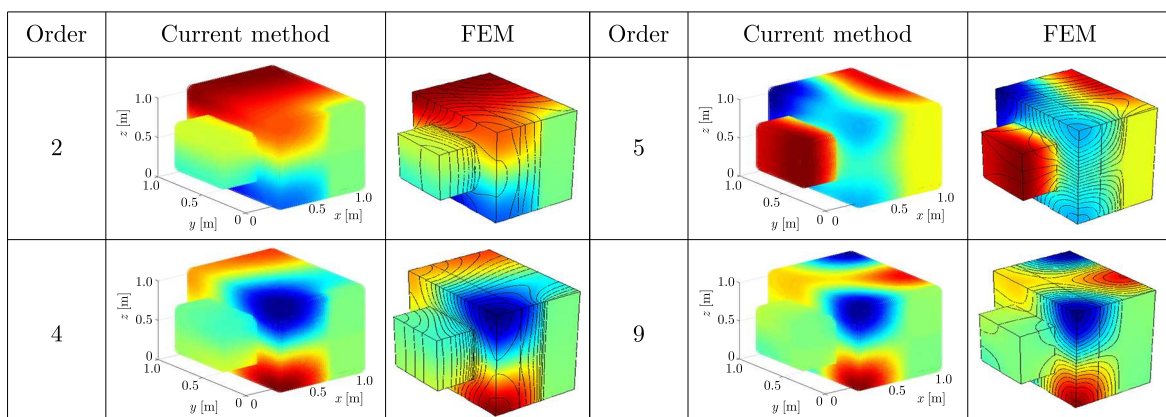


Fig. 2. Comparison of modal shapes of the acoustic system with the 2nd MPP

Through the above comparison, it is found that the results are in good agreement with FEM results, and it is proved that the current method can accurately predict the modal parameters of the acoustic system with the MPP at an arbitrary position. In addition, we also found that the MPP has a significant impact on sound pressure distribution, the sound pressure distribution is

no longer symmetrical, and the sound pressure is almost zero at the MPP position, which proves that the MPP can effectively absorb the sound energy.

Next, the heat release is introduced, with the parameters $b = 200$, $\tau = 0.002$ s. Two different acoustic structures are chosen as shown in Table 3. The right end of TAC₂ is the pressure release boundary. Table 3 shows a comparison between the modal frequency and growth rate calculated by the current method and FEM. The comparisons show that the modal frequency and growth rate are in good agreement, which proves the current method can accurately predict stability and corresponding thermoacoustic behavior characteristics of the 3D variable cross-sectional thermoacoustic coupling system.

Table 3. Parameters of cavity

Parameters of cavity 1	Parameters of cavity 2
$l_{x_1} = 0.2$ m, $l_{y_1} = 1$ m, $l_{z_1} = 1$ m	$l_{x_2} = 0.8$ m, $l_{y_2} = 1$ m, $l_{z_2} = 1$ m
$l_{x_1} = 0.2$ m, $l_{y_1} = 0.5$ m, $l_{z_1} = 0.5$ m	$l_{x_2} = 0.8$ m, $l_{y_2} = 1$ m, $l_{z_2} = 1$ m

Table 4. Comparison of frequency and growth rate of the thermoacoustic coupling system

Order	Cavity 1		Cavity 2	
	Frequency [Hz]	Growth rate [rad/s]	Frequency [Hz]	Growth rate [rad/s]
1	189.31 ^[a]	-12.99 ^[a]	98.52 ^[a]	-23.40 ^[a]
	189.33 ^[b]	-12.73 ^[b]	97.43 ^[b]	-22.29 ^[b]
2	189.31 ^[a]	-12.99 ^[a]	205.05 ^[a]	5.81 ^[a]
	189.39 ^[b]	-12.73 ^[b]	205.69 ^[b]	5.77 ^[b]
3	253.23 ^[a]	-34.62 ^[a]	205.05 ^[a]	5.80 ^[a]
	252.78 ^[b]	-34.61 ^[b]	205.69 ^[b]	5.77 ^[b]
4	254.67 ^[a]	-7.56 ^[a]	252.39 ^[a]	-59.38 ^[a]
	254.68 ^[b]	-7.27 ^[b]	253.54 ^[b]	-58.79 ^[b]
5	305.41 ^[a]	-24.48 ^[a]	264.79 ^[a]	1.70 ^[a]
	304.83 ^[b]	-25.36 ^[b]	265.19 ^[b]	1.94 ^[b]
6	305.41 ^[a]	-24.48 ^[a]	333.24 ^[a]	-2.18 ^[a]
	304.85 ^[b]	-25.18 ^[b]	334.17 ^[b]	-2.25 ^[b]

Remarks: ^[a] – current results, ^[b] – FEM results

3.2. Analysis of thermoacoustic coupling instability suppressed by the MPP

To explore the mechanism of the thermoacoustic coupling instability suppressed by the MPP separately and avoid energy dissipation of other impedance conditions, the straight and rigid cavity is preferred. The geometric parameters are $l_{x_1} = 0.6$ m, $l_{x_2} = 0.4$ m, $l_{y_1} = l_{y_2} = 0.3$ m, $l_{z_1} = l_{z_2} = 0.3$ m. First, it is necessary to master the behavior of the initial system, thus the modal frequency and growth rate of the thermoacoustic coupling system within 1000 Hz are predicted, see Fig. 3. It can be seen that there are 6 unstable modes in the first 1000 Hz of the thermoacoustic coupling system, and the instability of the low-order unstable modes is stronger.

Two unstable modes (176 Hz and 591 Hz) and two stable modes (337 Hz and 850 Hz) marked in Fig. 3 are selected, and the nondimensional sound pressures at $(0.8l_{x_2}, 0.5l_{y_2}, 0.5l_{z_2})$ are shown in Fig. 4. Figure 4a and 4c show the onset of nondimensional sound pressure for unstable modes, and the sound pressure increases exponentially with t . Figure 4b and 4d show the attenuation of nondimensional sound pressure of the stable modes, and the sound pressure gradually tends to zero with t . Since the modal growth rate -83.13 rad/s of 337 Hz is far less than the modal growth rate $-5.72\text{E-}5$ rad/s of 850 Hz, its modal sound pressure attenuation is significantly faster than in the 850 Hz mode.

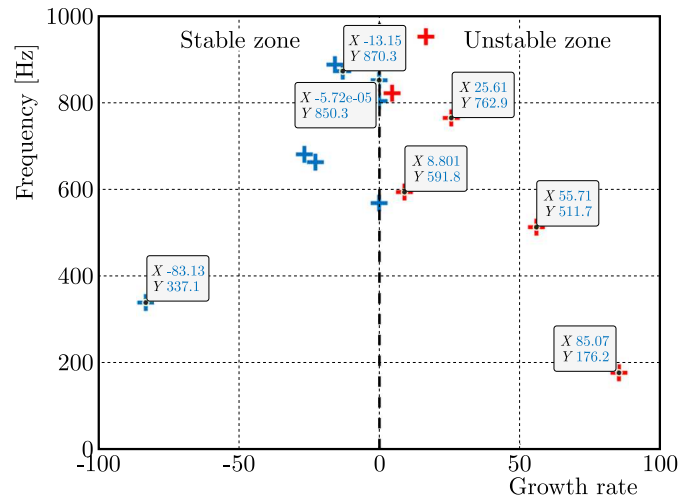


Fig. 3. Distribution of modal stability of the thermoacoustic coupling system without an MPP

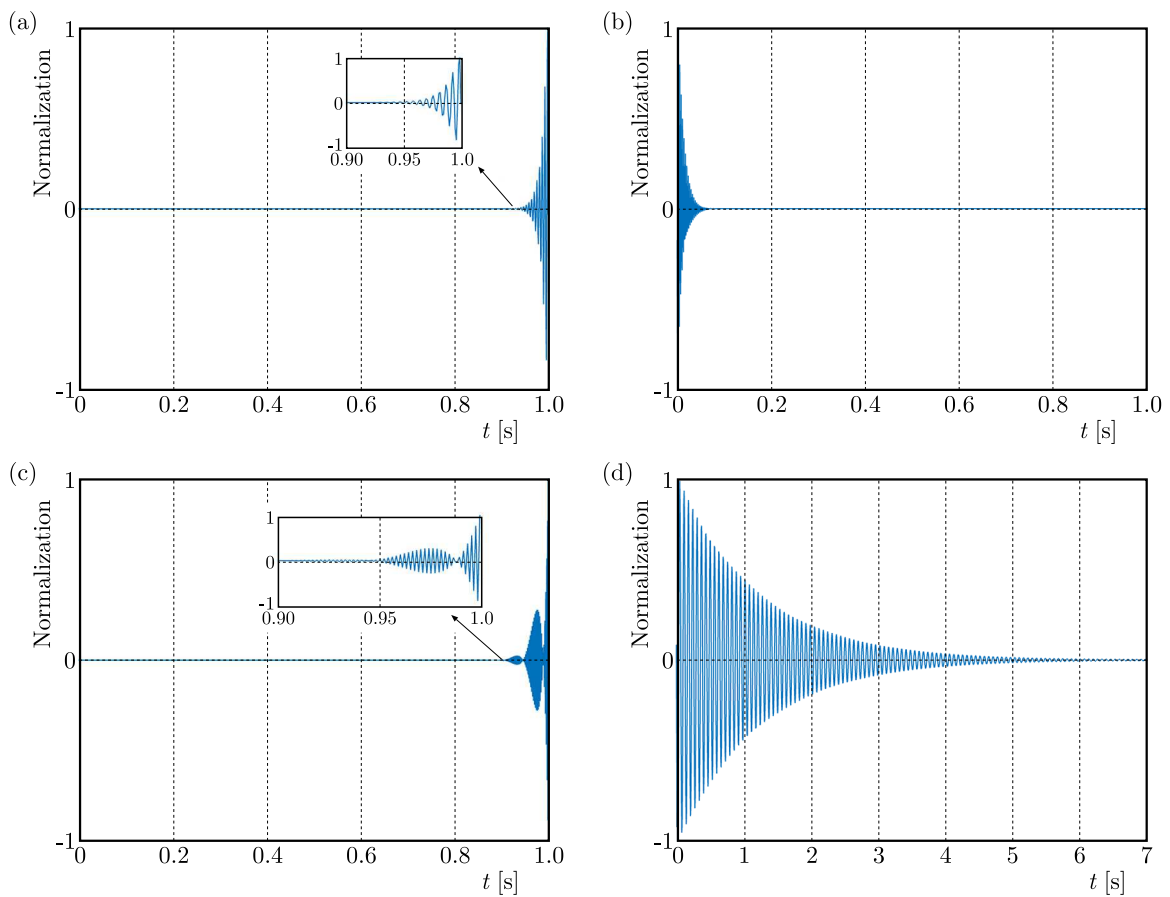


Fig. 4. The variation of nondimensional sound pressure for stable and unstable modes: (a) 175 Hz, (b) 337 Hz, (c) 591 Hz, (d) 850 Hz

Then, the MPP is introduced at $y = 0$ with the initial coordinates of $(0.7 \text{ m}, 0, 0)$, $l_{my} = 0.3 \text{ m}$, $l_{mz} = l_{z2}$. Figure 5 shows the modal frequency and stability distribution within the first 1000 Hz of the thermoacoustic coupling system with the MPP. Due to the introduction of MPP, the unstable modes are reduced from 6 orders to 4 orders, and the growth rates of still unstable modes are reduced to approaching the critical stable center with the zero growth rate, which

proves that the MPP can control the multi-order modes at the same time and enhance system stability.

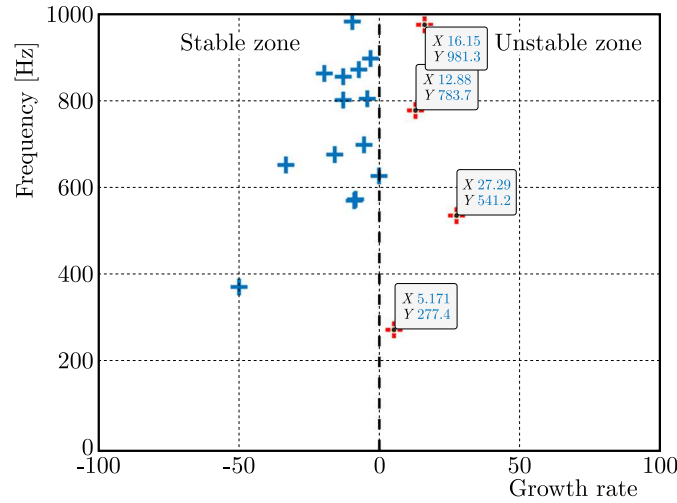


Fig. 5. Distribution of modal stability of the thermoacoustic coupling system with the MPP

Owing to the introduction of the MPP, the instability of the thermoacoustic coupling system is greatly modified, but the system is still not completely stable. This is because the MPP dissipates a part of the energy released by heat but fails to completely dissipate the energy generated by heat release. Therefore, it is necessary to further explore the effective set of the MPP on suppressing thermoacoustic instability.

3.3. Sound intensity distribution and energy transmission in the thermoacoustic coupling system

The thermoacoustic coupling process is essentially mutual conversion between thermal energy and acoustic energy. In order to clearly show the energy exchange characteristics between the heat source and the acoustic system, the sound pressure, sound intensity and its dispersion distribution of the thermoacoustic coupling system will be simulated separately. A combination of the sound intensity and dispersion can evaluate the energy transmission path, source and trap distribution law in the whole system, and provide an effective way to reveal the thermoacoustic characteristics and the instability control mechanism. The sound intensity energy and sound intensity divergence are defined as

$$I = \frac{1}{2}pu^* = S + jG \quad \text{div}(I) = \nabla(I) = \frac{\partial I_x}{\partial x} + \frac{\partial I_y}{\partial y} + \frac{\partial I_z}{\partial z} \quad (3.2)$$

where S is the active sound intensity, and G is the passive sound intensity.

To study the energy distribution of the thermoacoustic coupling system with/without an MPP, the parameters of acoustic cavity in Section 3.2 are selected. First, the sound pressure, sound intensity and divergence distribution of the thermoacoustic coupling system with/without the MPP are analyzed. The point source is introduced at $(0.3, 0.5l_{y1}, 0.5l_{z1})$, and the volume velocity is $2 \cdot 10^{-5} \text{ m}^3/\text{s}$. $y = 0.5ly$ section is chosen to observe the system characteristics. The excitation frequency is the 6 modal frequencies marked in Fig. 6.

Figure 6 shows a comparison of the passive sound intensity and sound pressure distribution of the acoustic system and the thermoacoustic system. In each figure, the upper subfigure shows characteristics of the acoustic system, and the lower subfigure shows characteristics of the thermoacoustic coupling system. The vector in the figure represents the passive sound intensity, and the color represents the sound pressure distribution. By comparing the passive sound intensity

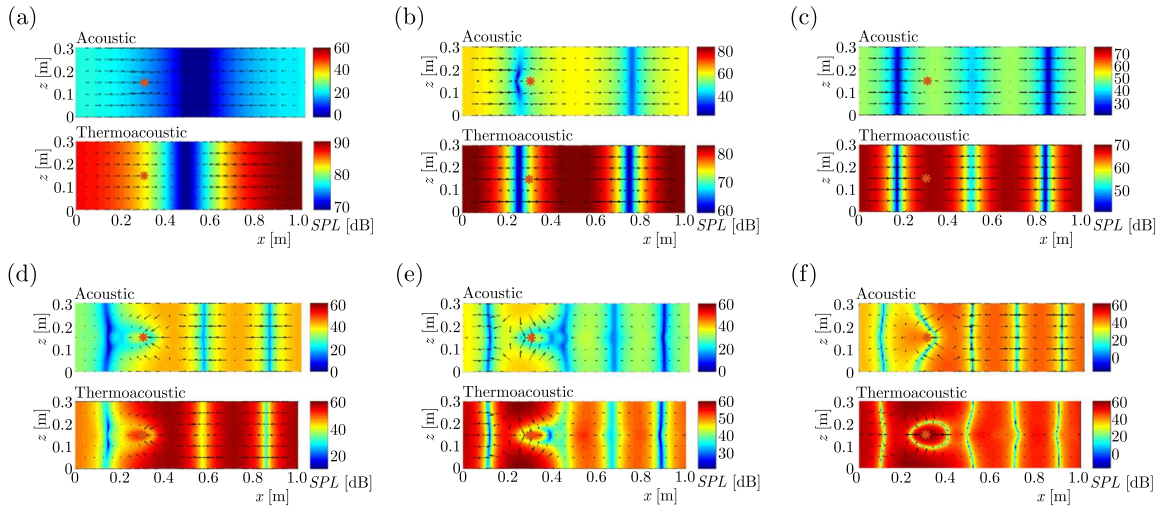


Fig. 6. Distribution of the passive sound intensity and sound pressure response: (a) 176.2 Hz, (b) 337.1 Hz, (c) 511.7 Hz, (d) 591.8 Hz, (e) 762.9 Hz, (f) 850 Hz

vector and sound pressure distribution in Fig. 6, it can be found that the passive sound intensity, as an oscillating energy flow, is always perpendicular to the isobaric surface of the sound field and parallel to the pressure drop direction. From the observation of the sound pressure distribution, it can be seen that the sound pressure response amplitude of the thermoacoustic system increases significantly, especially under a low frequency excitation. It means that the sound pressure of the system will be significantly enhanced after the introduction of the heat source.

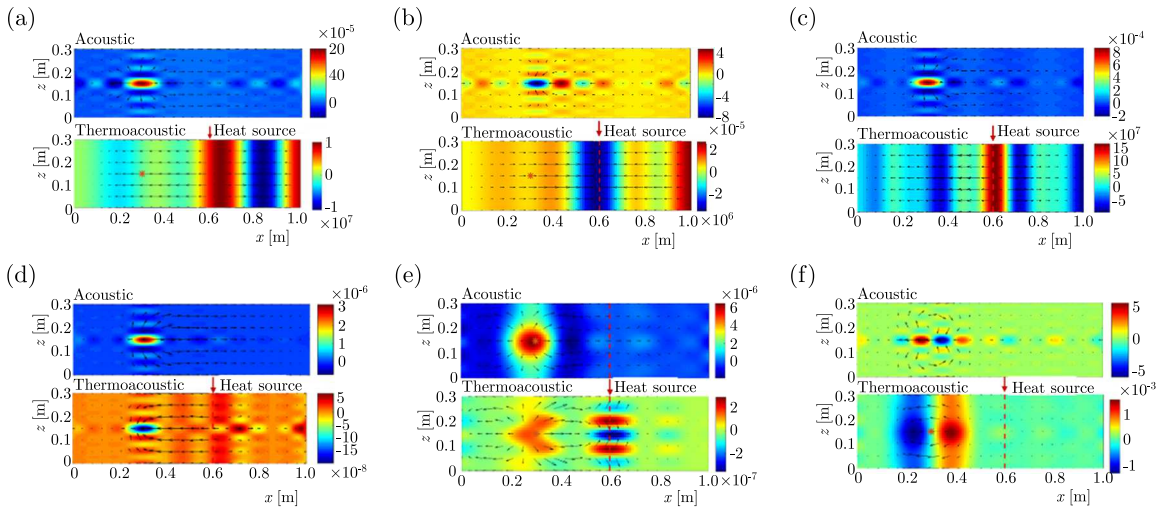


Fig. 7. Distribution of active sound intensity and divergence of the sound field: (a) 176.2 Hz, (b) 337.1 Hz, (c) 511.7 Hz, (d) 591.8 Hz, (e) 762.9 Hz, (f) 850 Hz

Figure 7 shows the active sound intensity and divergence of the system. The vector represents the active sound intensity, the color represents the sound intensity divergence. When the excitation frequency is an unstable mode frequency, as shown in Figs. 7a, 7c, 7d and 7e, there is a region with a divergence value greater than zero, and the energy is significantly increased compared with that in the non-heat source cavity system. By observing the sound intensity vector, we can see that the energy is transferred from the heat source to the whole sound field. It means that the heat source does positive work on the acoustic system, resulting in the system being in an unstable state. When the excitation frequency of the point source is a stable modal

frequency, as shown in Fig. 7b, the divergence near the heat source is negative, and the energy trap is near the heat source. The sound intensity vector shows that energy flows into the heat source position. Due to this phase, the energy generated by the heat source is opposite to the acoustic kinetic energy and potential energy, which reduces the energy of the acoustic system, so the system is in a stable state.

From the above analysis, the stability of the thermoacoustic coupling system depends on whether the heat source transmits energy to the acoustic system in the form of a source. The instability can be modified by adding energy-consuming elements in the thermoacoustic coupling system, blocking the transmission path of the energy source or reducing the energy transmission.

It can be seen from Fig. 7 that for unstable systems, the highest energy point is behind the heat source location rather than the heat source location. Therefore, before introducing the MPP, the energy concentration range of thermoacoustic unstable modes should be determined first. In order to fully cover the energy concentration area in Fig. 7, the MPP position was adjusted from $x_m = 0.7$ m to $x_m = 0.5$ m, and the length remained at $l_{my} = 0.3$ m. Figure 8 shows the distribution of modal stability within the first 1000 Hz of the thermoacoustic coupling system after only adjusting the MPP position. At this time, the unstable modes are all transformed into stable modes, indicating that the installation of the MPP at this position can effectively control the multimodal instability of the system.

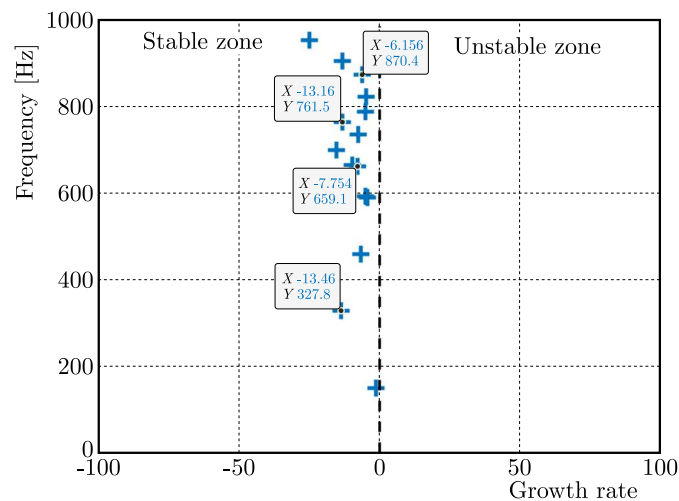


Fig. 8. Distribution of thermoacoustic system modal stability in 1000 Hz with MPP at 0.5 m

Figure 9 shows the passive sound intensity and sound pressure response distribution of the thermoacoustic coupling system under four excitation frequencies marked in Fig. 8. Compared with the amplitude of the sound pressure response at various excitation frequencies in Fig. 4, it can be found that the MPP not only transforms the unstable mode into a stable model, but also reduces the response to the acoustic disturbance. The active sound intensity and dispersion distribution are also shown in Fig. 10. It can be seen that the energy trap appears in the MPP area, the main energy in the system flows locally into the energy trap at the MPP. The MPP impedance blocks the way of the heat source transmitting energy into the system. The above analysis shows that the proper installation position of the MPP can suppress multi-mode instability in the thermoacoustic coupling system.

Finally, the above conclusion is applied to a variable cross-sectional thermoacoustic coupling system to further demonstrate the effectiveness of MPP in suppressing thermoacoustic instability. Cavity 2 in Table 3 is continuously used, where the modal characteristics are shown in Table 4. From Table 4, we can know that three modes are unstable in the first six modes. Then active/passive sound intensity, sound pressure and divergence distribution of the thermoacoustic

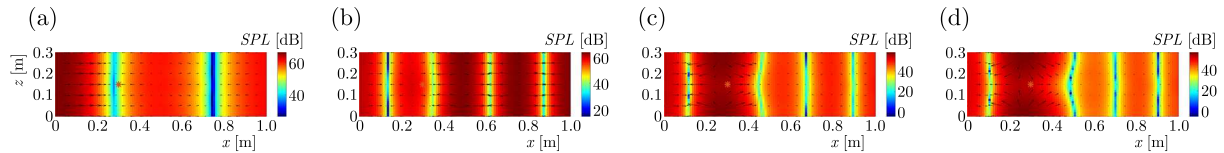


Fig. 9. Distribution of passive sound intensity and sound pressure of the sound field with the MPP at 0.5 m: (a) 327 Hz, (b) 659 Hz, (c) 761 Hz, (d) 870 Hz

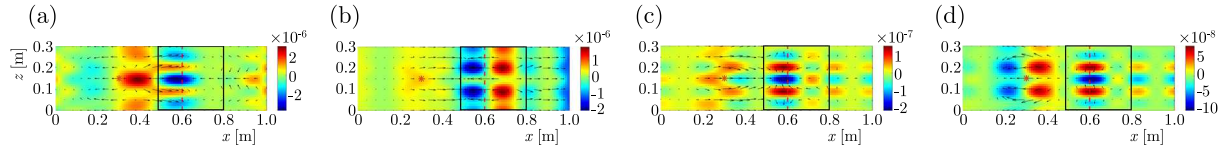


Fig. 10. Active sound intensity and divergence of the sound field with the MPP position at 0.5 m: (a) 327 Hz, (b) 659 Hz, (c) 761 Hz, (d) 870 Hz

system are given in Fig. 11 and 12. From these figures, it can be seen that the distribution of sound intensity, divergence and sound pressure are consistent with the above conclusion, where the passive sound intensity vector is always perpendicular to the isobaric surface of the sound field and parallel to the pressure drop direction, and the heat source does positive work in the unstable thermoacoustic system.

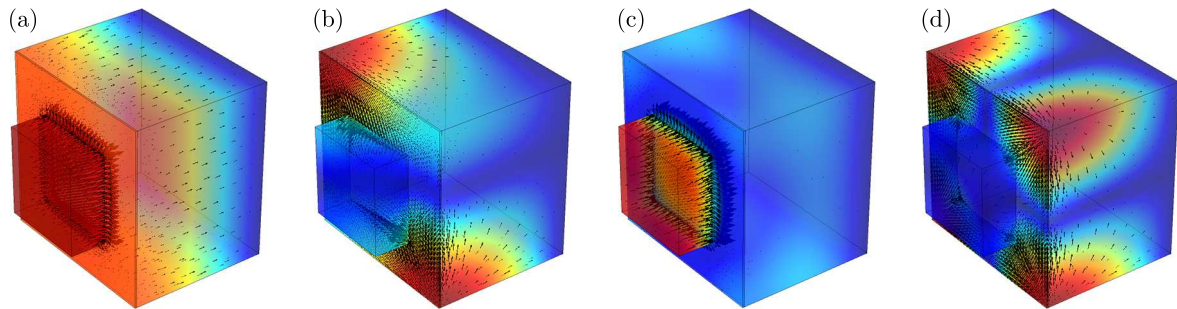


Fig. 11. Passive sound intensity and sound pressure of the variable cross-sectional thermoacoustic system: (a) 98.52 Hz, (b) 205.05 Hz, (d) 252.39 Hz, (e) 264.79 Hz

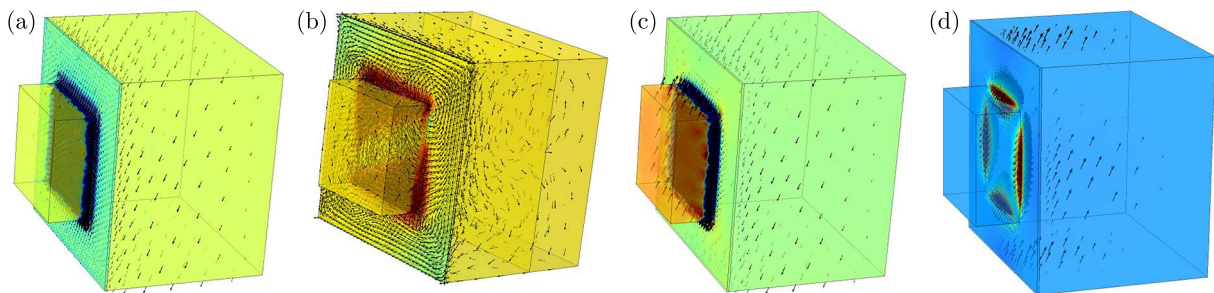


Fig. 12. Active sound intensity and divergence of the variable cross-sectional thermoacoustic system: (a) 98.52 Hz, (b) 205.05 Hz, (d) 252.39 Hz, (e) 264.79 Hz

The MPP is introduced on all six walls at $x_m = 0.2$ m to $x_m = 0.7$ m, which means that the length of the MPP is 0.5 m. Figure 13 shows the distribution of system stability before/after the introduction of MPP. Successfully, the unstable modes are all transformed into stable modes, indicating that the installation of the MPP can effectively control the multimodal instability of the system.

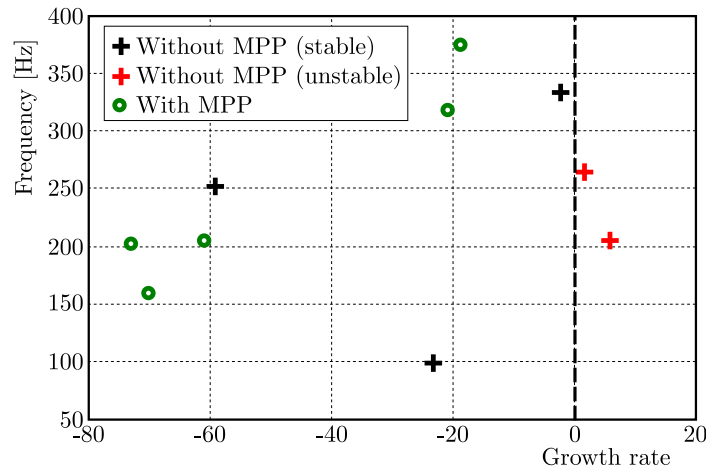


Fig. 13. Modal stability of the variable cross-sectional thermoacoustic system with/without MPP

4. Conclusion

A 3D variable cross-sectional thermoacoustic coupling model with an MPP is established. By a substructure method, the complex cavity is divided into acoustic cavity substructures and auxiliary air plates. The 3D modified Fourier series is used to characterize the sound pressure distribution function in the cavity to meet arbitrary impedance boundary conditions, so that the sound pressure distribution function and its derivatives can be continuously guided in the acoustic field solution domain. The energy formulas of each acoustic cavity substructure and auxiliary air plate are derived, and the modal frequency, growth rate, and corresponding sound pressure, sound intensity and divergence distribution are obtained by using the Lagrange equation and Rayleigh-Ritz method. The main conclusions are as follows:

- The modal characteristics of the thermoacoustic coupling system with the MPP are analyzed. The results show that the MPP can suppress multi-mode instability and improve stability of the thermoacoustic coupling system.
- The dimensionless sound pressure of unstable modes is exponentially amplified with time, and the nondimensional sound pressure of stable modes decay to zero with time. The sound pressure of more stable modes decays faster.
- The distribution of energy transmission path, source and trap is determined based on the sound intensity and divergence. The introduction of a heat source makes the sound pressure response amplitude increase significantly and the variation of divergence distribution more complex. Under the excitation of an unstable mode frequency, the heat source transmits energy to the sound field. Under the excitation of a stable mode frequency, the energy near the heat source is an energy trap, and the energy in the sound field flows into the vicinity of the heat source.
- It is revealed that stability of the thermoacoustic coupling system depends on whether the heat source transmits energy to the acoustic system or not. The instability of the system can be modified by blocking the transmission path or reducing energy transmission. The suppression of multimodal instability of the thermoacoustic coupling system can be achieved and the acoustic disturbance response of the system can be effectively reduced when the MPP is adjusted to the energy concentration area.

Acknowledgments

This work was supported by Marine Power Research and Development (Grant No. DE0305); and the National Natural Science Foundation of China (Grant No. 11972125 and 12102101).

References

1. ARMITAGE C.A., RILEY A.J., CANT R.S., *et al.*, 2004, Flame transfer function for swirled LPP combustion from experiments and CFD, *Proceedings of the ASME Turbo Expo 2004: Power for Land, Sea, and Air*, Vol. 1: Turbo Expo, 527-537
2. CHU M., XU X., 2016, Acoustic numerical simulation of a micro-perforated panel absorber for combustion instability suppression, *Acta Acoustica*, **41**, 2, 236-242
3. DOWLING A.P., MAHMOUDI Y., 2015, Combustion noise, *Proceedings of the Combustion Institute*, **35**, 1, 65-100
4. DU J.T., LI W.L., LIU Z.G., XU H.A., JI Z.L., 2011, Acoustic analysis of a rectangular cavity with general impedance boundary conditions, *Journal of the Acoustical Society of America*, **130**, 2, 807-817
5. ELDREDGE J.D., DOWLING A.P., 2003, The absorption of axial acoustic waves by a perforated liner with bias flow, *Journal of Fluid and Mechanics*, **485**, 307-335
6. LEFEBVRE A.H., BALLAL D.R., 2010, *Gas Turbine Combustion*, CRC Press, 525
7. LEYKO M., NICOU D., POINSOT T., 2012, Comparison of direct and indirect combustion noise mechanisms in a model combustor, *American Institute of Aeronautics and Astronautics Journal*, **47**, 11, 2709-2716
8. MA D.Y., 1975, Theory and design of micro-perforated panel sound absorption structure, *Scientia Sinica*, **1**, 38-50
9. SCHÖNFELD T., POINSOT T., 1999, Influence of boundary conditions in LES of premixed combustion instabilities, *Center for Turbulence Research Annual Research Briefs*, 73-84
10. SCHULLER T., DUROX D., CANDEL S., 2003, Self-induced combustion oscillations of laminar premixed flames stabilized on annular burners, *Combustion and Flame*, **135**, 4, 525-537
11. SEO S., 2003, Combustion instability mechanism of a lean premixed gas turbine combustor, *Journal of Mechanical Science and Technology*, **17**, 6, 906-913
12. SUN X.F., 2010, Thermoacoustic oscillating calculation of longitudinal equivalence frequency and stability in aero-engine afterburner, <https://api.semanticscholar.org/CorpusID:111882612>
13. ZHANG X.Q., 2020, *Acoustic Behavior of Micro-Perforated Panels in Grazing Flow*, The Hong Kong Polytechnic University

Manuscript received February 17, 2023; accepted for print June 28, 2023